Coaxial multishell nanowires with high-quality electronic interfaces and tunable optical cavities for ultrathin photovoltaics

Thomas J. Kempa[a,1], James F. Cahoon[a,1,2], Sun-Kyung Kim[a,b], Robert W. Day[a], David C. Bell[c], Hong-Gyu Park[b,3], and Charles M. Lieber[a,c,3]

[a]Department of Chemistry and Chemical Biology, Harvard University, Cambridge, MA 02138; [b]Department of Physics, Korea University, Seoul 136-701, Republic of Korea; and [c]School of Engineering and Applied Sciences, Harvard University, Cambridge, MA 02138

Silicon nanowires (NWs) could enable low-cost and efficient photovoltaics, though their performance has been limited by nonideal electrical characteristics and an inability to tune absorption properties. We overcome these limitations through controlled synthesis of a series of polymorphic core/multishell NWs with highly crystalline, hexagonally-faceted shells, and well-defined coaxial p-type/n-type (p/n) and p/intrinsic/n ($p/i/n$) diode junctions. Designed 200–300 nm diameter $p/i/n$ NW diodes exhibit ultralow leakage currents of approximately 1 fA, and open-circuit voltages and fill-factors up to 0.5 V and 73%, respectively, under one-sun illumination. Single-NW wavelength-dependent photocurrent measurements reveal size-tunable optical resonances, external quantum efficiencies greater than unity, and current densities double those for silicon films of comparable thickness. In addition, finite-difference-time-domain simulations for the measured NW structures agree quantitatively with the photocurrent measurements, and demonstrate that the optical resonances are due to Fabry-Perot and whispering-gallery cavity modes supported in the high-quality faceted nanostructures. Synthetically optimized NW devices achieve current densities of 17 mA/cm^2 and power-conversion efficiencies of 6%. Horizontal integration of multiple NWs demonstrates linear scaling of the absolute photocurrent with number of NWs, as well as retention of the high open-circuit voltages and short-circuit current densities measured for single NW devices. Notably, assembly of 2 NW elements into vertical stacks yields short-circuit current densities of 25 mA/cm^2 with a backside reflector, and simulations further show that such stacking represents an attractive approach for further enhancing performance with projected efficiencies of >15% for 1.2 μm thick 5 NW stacks.

nanodevices | nanomaterials | nanophotonics | optical nanocavities | solar cells

Nanostructures and nanostructured materials may enable next-generation solar cells by providing for efficient charge separation (1–16) and tunable optical absorption (11, 17–19). Semiconductor nanowires (NWs) have exhibited promising efficiencies as single NW photovoltaic elements (8–11, 20–22) and as vertical arrays configured as photovoltaic (23–26) and photoelectrochemical (27, 28) solar cells, where the vertical array has been used to enhance light absorption (29). In the case of Si-based nanostructures, where Si photovoltaics represent benchmark systems with attractive material abundance and cost (30), the efficiency of NW devices has typically been limited by poor electrical performance and lack of tunable control of absorption properties at specific and broadband wavelengths. For example, previous reports of coaxial (8) and axially modulated (9) p-i-n single-NW photovoltaic devices yielded open-circuit voltages (V_{OC}) below 0.29 V, and, for coaxial devices, large leakage currents >1 pA. Furthermore, to accurately identify potentially unique absorption modes through photocurrent spectra and simulations, photonic devices must exhibit high-quality and reliable electrical characteristics, unlike previous devices (8). Vertical

arrays of micron-diameter wires have shown better performance characteristics, yielding V_{OC} values of 0.50–0.56 V (19–21). However, preparation of microwire-based high V_{OC} photovoltaics (22) and photocathodes (29) has utilized high-temperature growth, dopant diffusion, and/or annealing processes (temperatures of 850–1000 °C), which limit precise structural control and involve high thermal cost. Here, we report bottom-up synthesis of a unique class of core/multishell Si NWs that overcome the limitations typically encountered in nanoscale Si devices. In situ synthetic control of structural morphology, size, and doping provides a method to design rationally and tune the properties of these nanostructures. Furthermore, we establish the importance of strong optical resonances for controlling absorption in the small, 200–300 nm diameter, NW cavities. This latter feature is distinct from the behavior in micro-wires and suggests NW structures as promising building blocks for new photonic and solar cell devices.

Results and Discussion

To probe key structural characteristics dictating the electronic and optical properties of these NWs, we designed, synthesized, and characterized four distinct coaxial Si NW structures (Fig. 1*A*), in which doping in core and shell regions was varied in situ. We label these core/shell structures p/n, p/in, p/pn, and p/pin according to the sequential doping of the core/shells, where p, i, and n refer to p-type, intrinsic, and n-type, respectively, and the structures all share a common p-type Si NW core. Our synthetic protocol (see *Materials and Methods*) uses metal nanocluster-catalyzed, vapor-liquid-solid (VLS) growth for the p-Si NW core growth followed by vapor-solid (VS) growth of the shells. The thicknesses of the p, i, and n-type shells were controlled precisely by growth time using independently characterized growth rates (see *Materials and Methods*). A representative field-emission scanning electron microscopy (SEM) image of a p/in coaxial Si NW (Fig. 1*B*) shows clear faceting with smooth facet surfaces distinct from the disordered and unfaceted nanocrystalline Si morphology reported previously (8). We note that clear faceting with smooth facet surfaces was achieved for each of the four types of coaxial structures (Fig. S1) and is indicative of highly crystalline shells in our NW structures.
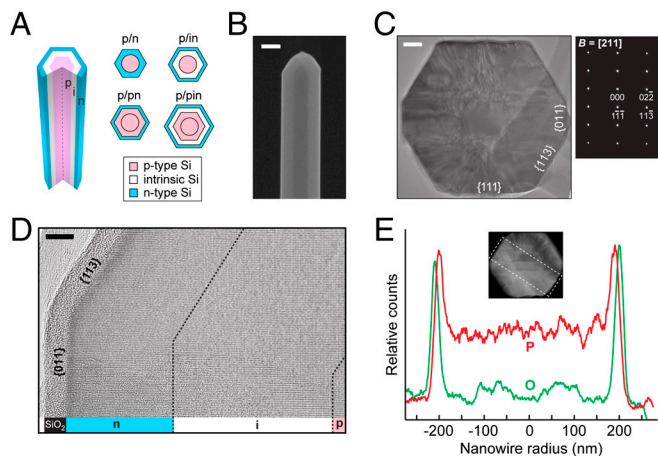
Fig. 1. Design, synthesis, and characterization of polymorphic core/multishell NWs. (*A*) Three dimensional schematic of a typical core/shell NW and cross-sectional schematics of four core/shell diode geometries investigated as standalone single-NW solar cells. (*B*) SEM image of an as-grown, core/shell *p/in* Si NW; scale bar, 100 nm. (*C*) *Left*: bright-field TEM image of a NW cross-section showing a core surrounded by crystalline shell; scale bar, 50 nm. *Right*: electron diffraction pattern for the cross-section on left showing it is oriented along the [112] zone axis. (*D*) High-resolution bright-field, aberration-corrected TEM image at the {011}, {113} vertex of a NW cross-section revealing clear lattice fringes; scale bar, 5 nm. (*E*) Phosphorous (red) and oxygen (green) line profiles across a NW cross-section acquired from EDS elemental mapping on an aberration-corrected STEM. *Inset*: cs-STEM image of NW cross-section from which data was taken; scale bar, 100 nm.

To elucidate the crystalline structure of the core/shell NWs we have used high-resolution transmission electron microscopy (TEM) to image cross-sectional samples (see *Materials and Methods*). A representative bright-field image of a *p/pin* multishell structure (Fig. 1*C*) shows several key features. First, the shell of this *p/pin* structure consists of several distinct domains ordered about the approximately 100 nm diameter NW core. Second, the electron diffraction pattern recorded from this sample yields clean, sharp spots characteristic of uniform diffraction from the [112] zone axis of the cubic Si crystal structure. These data show that the core and shell are coherently oriented in the ⟨112⟩ direction and thus indicate that the domains in the shell are separated by twist grain boundaries which preserve this direction. Third, lattice-resolved TEM images recorded near the outer region of the sample (Fig. 1*D*) show clear (111) lattice fringes up to the amorphous SiO_2 coating at the outermost edge of the NW. Also, on the basis of these images, surfaces of the NW can be assigned to two {111} planes, two {011} planes, and four {113} planes. Taken together, the TEM data and analysis suggest a unique, polymorphic shell structure composed of crystalline domains, which maintain coherent faceting and ⟨112⟩ crystal orientation along the length of the coaxial *p/pin* NW.

In addition, energy dispersive X-ray spectroscopy (EDS) was used to characterize the phosphorous dopant and oxygen profiles in a *p/pin* core/shell cross-sectional sample (Fig. 1*E*, and see *Materials and Methods*). The oxygen profile exhibits two peaks at the left and right edges of the sample arising from the SiO_2 layer on the faceted surfaces of the NW *n*-shell. The phosphorous profile also exhibits two peaks coincident with the left and right sides of the outer *n*-shell, which are shifted by 10–15 nm with respect to oxygen and have peak widths, 20–30 nm, in good agreement with the expected *n*-shell thickness of 25 nm based on measured growth rates. The relatively large apparent background signal in the phosphorous profile is an artifact resulting from mixed Si and P signals (Fig. S2). These measurements verify the capability to synthetically encode well-defined, nanoscale dopant variations in core/shell NWs and represent the first successful effort at mapping active dopants in complex NW structures. To-

gether, these characterization results verify the synthesis of a new NW motif possessing precisely defined nanometer-scale doped regions and a tunable crystal morphology.

Electrical transport properties of the four distinct classes of coaxial NWs were measured by fabrication of single NW devices with electrical contacts selectively defined to the *p*-type core and *n*-type shell (Fig. 2*A*, and see *Materials and Methods*). All current-voltage (*I* − *V*) characteristics (Fig. S3) were measured under air-mass 1.5 global (AM 1.5 G) 1-sun (100 mW/cm²) illumination, with current density (*J*) calculated using the projected NW area (8, 22, and see *Materials and Methods*). The illuminated *J* − *V* curves corresponding to each of the four distinct coaxial NW device structures (Fig. 2*B*) show progressive changes in V_{OC} and reveal several important features. First, the highest V_{OC} value, 0.48 V, is obtained for the *p/in* geometry and represents a substantial, twofold improvement over our previous coaxial NWs with nanocrystalline shells (8), and is the highest V_{OC} reported to date for a single Si NW device. We have attained V_{OC}'s >0.47 V from devices with diameters as small as 200 nm, showing that much larger micron-scale diameters (22) are not necessary to achieve good performance. Second, the *p/in* device exhibits a fill factor (FF) of 73%, substantially higher than the 55% FF reported previously (8). The high FF combined with the steep slope of the *J* − *V* curve at V_{OC} are clear signatures of negligible series resistance in these devices. Third, for similar crystalline quality coaxial nanowires, the insertion of an approximately 30 nm intrinsic layer causes 140 mV (*p/n* to *p/in*) and 40 mV (*p/pn* to *p/pin*) improvements in V_{OC}. To further assess the control of junction properties in these core/multishell NWs, we examined the junction leakage current for the four distinct types of structures. A
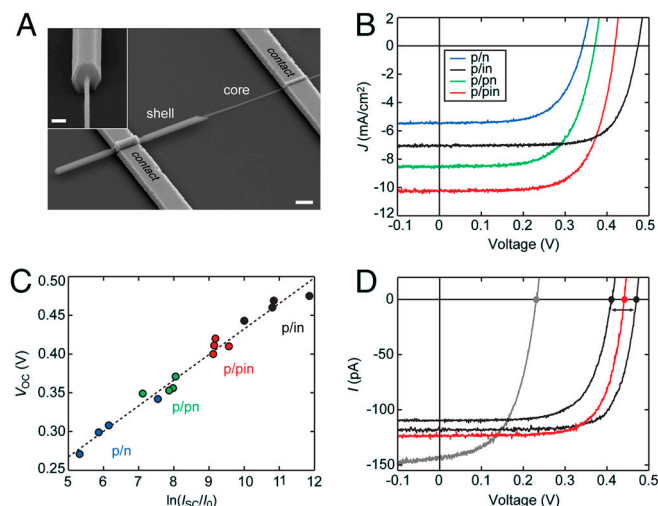

Fig. 2. Transport properties of single-NW solar cells. (*A*) SEM image of a standalone NW device with lithographically defined Ti/Pd contacts overlapping the shell and core regions of the NW; scale bar, 1 μm. *Inset*: SEM image of a single core/shell NW transferred onto a Si_3N_4 substrate and wet-chemically etched on the lower portion to reveal the core; scale bar, 200 nm. (*B*) Current density-voltage (*J* − *V*) characteristics of single-NW solar cells composed of four distinct diode geometries (refer to Fig. 1*A*). (*C*) Open-circuit voltage (V_{OC}) versus the logarithm of the ratio of short-circuit current (I_{SC}) to dark saturation current (I_0) for the four best devices from each diode geometry. A fit (dashed line) to the ideal diode equation yields an ideality factor $n = 1.28$. This value is lower than those calculated from dark *I* − *V* data for individual devices, although we note that our values for n (1.3–1.8) indicate consistently the presence of carrier recombination within the depletion region of all devices. (*D*) Current-voltage characteristic (red) for a *p/in* NW device for which Au catalyst was removed by aqueous KI/I_2 wet-chemical etch prior to shell growth. Gray curve is for an *i/pin* Si NW device whose growth was catalyzed by Al. Black curves show current-voltage characteristics for a single Au-catalyzed *p/in* NW device measured before and after oxidation of its surface in air for one week.

Kempa et al.

plot of V_{OC} versus the logarithm of the ratio of short-circuit current (I_{SC}) to dark saturation current (I_0) for sixteen total devices (Fig. 2C) is linear, as expected, with a monotonic increase in V_{OC} with decreasing I_0 (31, and see *Materials and Methods*). Significantly, the *p/in* device with $V_{OC} = 0.48$ V has a dark saturation current $I_0 = 1.1$ fA and current density $J_0 = 0.34$ fA/μm^2, which represents a 1000-fold improvement over our previous nanocrystalline-shell NW devices (8). The dramatic reduction in leakage current directly correlates with the twofold improvement in V_{OC}. These data further support our conclusion that the synthetic control of NW structure has enabled improvements in all electronic metrics, V_{OC}, FF, I_0, relevant to photovoltaic devices.

Several groups have also postulated that metal nanocluster catalysts, especially gold, used to grow NWs could enhance recombination and adversely affect V_{OC} in NW devices (32). Although our V_{OC} values for Au-nanocluster catalyzed NWs already suggest a level of material quality approaching that of good planar Si devices (see *Materials and Methods*), we have further investigated this point. First, NWs were synthesized using Al (Fig. S4) as the metal catalyst (32) because Al, unlike Au, does not act as a midband gap trap state in Si (33). Notably, the best illuminated $I - V$ curve for a *p/pin* diode geometry (Fig. 2D, gray curve) yields a V_{OC}, 0.23 V, approximately two times smaller than the value for analogous Au-catalyzed devices. Second, removal of Au catalysts from as-grown NW cores (see *Materials and Methods*) to preclude incorporation of Au during the higher temperature shell growth steps (Fig. 2D, red curve) yielded a device with V_{OC}, 0.44 V, similar to our best results for coaxial NWs prepared without removal of the catalyst. Together, these results show that proposed Au impurities do not adversely lower V_{OC}, and suggest that the overall quality of the core/multishell structure is more important for our NW devices. In addition, measurements made before and after passivation of the outermost *n*-shell (black curves, Fig. 2D) show that surface oxidation yields an approximately 58 mV increase in V_{OC}, suggesting that surface recombination has only a small effect on the overall V_{OC} of our best coaxial NW devices. In summary, comparisons among the four classes of polymorphic core/multishell NWs as well as with previous core/nanocrystalline-shell NWs (8) demonstrate that our in situ synthetic control enables realization of optimized *p/in* and *p/pin* NW structures with high electrical performance as manifest by the substantially improved V_{OC}, FF, and I_0 values.

The *p/in* and *p/pin* core/multishell NW devices (Fig. 2B) also exhibit J_{SC} values, 8–10 mA/cm^2, substantially larger than expected for an equivalent thickness of bulk Si (31). Data obtained on NW devices with lengths spanning over 1 order of magnitude (Fig. S5) exhibit linear scaling of I_{SC} and nearly constant J_{SC}, suggesting that the high J_{SC} values are intrinsic to these nanoscale structures and are not due to extrinsic factors such as scattering by contact electrodes (8). To understand the origin of these large J_{SC} values, we carried out wavelength-dependent photocurrent measurements and finite-difference time-domain (FDTD) simulations on individually characterized core/multishell NW devices (see *Materials and Methods*). A representative curve of the absolute external quantum efficiency (EQE) versus wavelength acquired for a *p/in* NW device (Fig. 3A, black curve; Fig. S6) and the corresponding simulated EQE spectrum (Fig. 3A, red dashed curve) demonstrate several important points. First, the experimental and simulated spectra are highly structured, with very good agreement in the peak positions. Significantly, from analysis of the simulations and polarization-dependent experiments (Fig. S6) we can assign peaks in EQE to wavelength-dependent Fabry-Perot (Fig. 3 labels 1, 2, 4, and 5) and whispering-gallery (Fig. 3 labels 3 and 6) resonant absorption modes within the hexagonal NW structure. Second, there is excellent correspondence in absolute EQE amplitudes between experiment and simulation, where the full-field FDTD simulations are executed without adjustable parameters and assume that internal
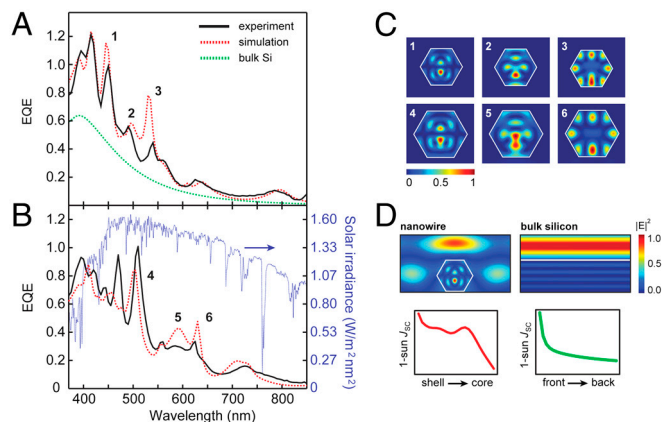

Fig. 3. Enhanced and tunable absorption in NWs. (*A*) External quantum efficiency (EQE) as a function of wavelength for a *p/in* NW (black curve) and simulated EQE spectrum (dashed red curve) produced with no adjustable parameter other than the size of the NW (height of 240 nm). Dashed green curve shows the simulated spectrum for top 240 nm of planar bulk Si. (*B*) EQE spectrum (black curve) of a *p/pin* NW compared to the irradiance of the AM1.5G solar spectrum (dashed blue curve). Dashed red curve corresponds to simulated EQE calculated with no other adjustable parameter besides the NW size (height of 305 nm). (*C*) FDTD simulations of resonant mode spatial profiles for *p/in* (profiles 1–3) and *p/pin* (profiles 4–6) structures. Labeled profiles correspond to the EQE peaks labeled identically within Fig. 3 *A–B* and profiles in each column correspond to the same mode excited within both structures. All profiles are for TM polarizations and use a linear color scale representing absorption (not electric field intensity) within the mesoscopic structures. Resonant modes labeled 3 and 6 correspond to whispering-gallery type modes while all others correspond to Fabry–Perot resonances. (*D*) Plot of electric field intensity for plane wave ($\lambda = 445$ nm) interacting with a NW (*Left*) and bulk Si (*Right*). White line defines outline of NW and top surface of bulk Si. Beneath are plots of total J_{SC} as a function of position inside the NW or bulk Si.

quantum efficiency (IQE) has value of unity (see *Materials and Methods*). This agreement in amplitudes further supports the use of NW projected area in calculation of current densities, and moreover, indicates that charge recombination is minimized in our new *p/in* and *p/pin* core/multishell structures. Third, the EQE spectrum approaches and even exceeds unity for wavelengths in the range of 400–500 nm. EQE values greater than unity are possible because of an optical antenna effect (17, 18), in which the absorption cross-section of the NW exceeds its physical cross-section for some photon energies. This phenomenon is a purely classical effect caused by the subwavelength diameter of the NW and is quantitatively reproduced by the FDTD simulations.

To illustrate how rational synthetic design can be used to tune absorption within our NW photovoltaic elements, we examined a larger diameter (305 vs. 240 nm) *p/pin* NW device. The measured and simulated absolute EQE spectra for the *p/pin* device (Fig. 3B, Fig. S6C) exhibit several features differentiating them from the corresponding spectra discussed above for the *p/in* NW device. First, peaks 4–6 in the *p/pin* spectrum (Fig. 3B), which correspond to the same modes (Fig. 3C) represented by peaks 1–3 in the *p/in* spectrum (Fig. 3A), are substantially red-shifted. Second, the *p/pin* device exhibits a larger number of peaks in the experimental and simulated EQE spectra. Third, the *p/pin* experimental spectrum (Fig. 3B) exhibits two peaks between 470 and 520 nm with near-unity amplitudes. These two peaks correspond to resonant modes localized near the core-shell interface (Fig. 3C, label 4). We suggest that the higher than predicted EQE values may result from enhanced absorption within the first approximately 20 nm of the polymorphic *p*-shell surrounding the *p*-core, although future studies will be needed to confirm and potentially exploit these differences in detail. The observed red-shifted modes with enhanced absorption are also better matched in frequency to the maximum irradiance of the solar spectrum (Fig. 3B,

CHEMISTRY

blue dashed curve). This observation explains the approximately 40% larger J_{SC} of p/pin NWs compared to p/in NWs (Fig. 2B), and underscores our ability to optimize device performance through synthetic tuning of nanostructures.

We also compared the experimental and simulated optical properties of a p/in core/multishell NW (Fig. 3A) to an equivalent thickness of bulk Si. The simulated EQE spectrum for 240 nm of bulk Si (Fig. 3A, dashed green line) is featureless and shows substantially lower amplitude than the p/in NW. The origin of the differences in EQE spectra can be understood by comparing the interaction of light with both structures. For example, a plot of the electrical field intensity for an incident plane wave with a wavelength of 445 nm (Fig. 3D) shows a strong resonant mode excited within the NW, but the profile of electric field within an equivalent thickness of bulk Si is featureless. These modes in the NWs lead to substantial and structured J_{SC} contribution from the shell through much of the core, while bulk Si exhibits the standard exponential decay as function of thickness (Fig. 3D). Significantly, the spatial localization and intensity of resonant modes could be adjusted by tuning the morphology of the NW cavity.

The studies discussed above demonstrate substantial improvement in the photovoltaic properties of Si NWs at the single-NW level. To determine whether J_{SC} could be improved further, we fabricated NW devices on transparent quartz substrates and measured $J - V$ characteristics with and without a silver metal back-side reflector (BSR), as shown in Fig. 4A. Without the BSR, a representative single p/pin device (red line) yields $J_{SC} = 9.8$ mA/cm² and an overall conversion efficiency, η, of 3.2%. Significantly, the same device with a BSR yields $J_{SC} = 17.0$ mA/cm² and $\eta = 5.9\%$. The substantial increase in efficiency achieved with the BSR thus suggests one straightforward route to mitigate incomplete absorption and thereby enable efficient nanowire-based solar cells.

While individual NW photovoltaics represent the ideal platform for elucidating fundamental factors affecting device effi-

ciency and can be used to power nanoelectronic elements (8), it is also important to consider the prospects for scaling these to arrays that will be required for solar cells. As an initial step in this direction we interconnected in parallel from 1 to 8 p/pin core/multishell NW elements. Measurements of light $I - V$ data from these small multi-NW devices (Fig. 4B, Inset) show good "cell" characteristics are maintained (e.g., V_{OC} and FF are nearly constant) with increasing number of NW elements. Indeed, the FF for the 8 NW device, 69.3%, is similar to the best value we achieved on single NW elements, 68.0%. Moreover, and central to the potential for scaling, we observe a stepwise increase in I_{SC} from 191 to 1723 pA as the number of NWs in a device is increased from 1 to 8, respectively (Fig. 4B). Importantly, this increase in absolute I_{SC} is also accompanied by preservation of J_{SC} to within 3% of that for the best single NW device. We believe these results show that assembly and large-scale integration could be a viable strategy for using our core/multishell nanowire building blocks, although future studies will be required to expand to larger arrays. Such work should be able to exploit reported advances in assembly of dense parallel nanowires on the micrometer to several inch scale (34), where the nanowires have also exhibited good electronic properties (34, 35).

Furthermore, we propose and describe here a unique paradigm for significantly enhancing current density and thereby efficiency, which involves layering and interconnecting designed coaxial core/multishell NW components. To demonstrate this unique concept we have assembled vertical stacks of horizontally oriented NW devices (see *Materials and Methods*). A representative SEM image of the assembled NWs (Fig. 5A, Inset) shows the well-aligned vertical stack of two p/pin NWs on a quartz sub-
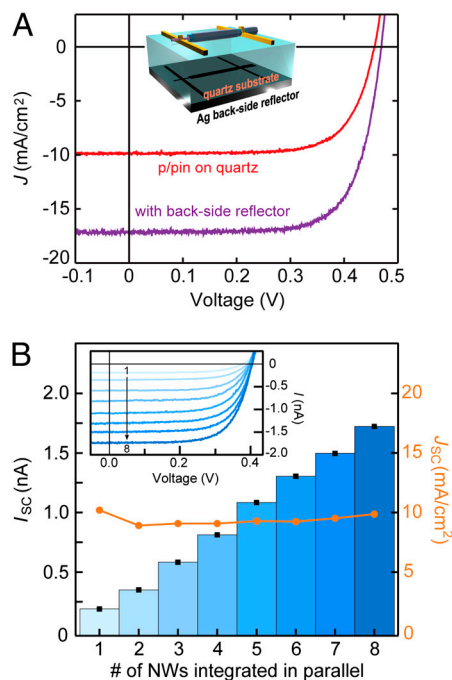

Fig. 4. Integration of NW components for efficient solar cells. (A) Current density-voltage ($J − V$) characteristics for a p/pin device without (red curve) and with a Ag back-side reflector (purple curve) under 1-sun illumination. Inset: schematic of the device layout on quartz. (B) Linear scaling of I_{SC} (black squares and shaded blue bars) and preservation of J_{SC} (orange circles and line) as multiple p/pin NWs are integrated in parallel. Inset: light $I − V$ curves for devices consisting of 1–8 NWs connected in parallel.
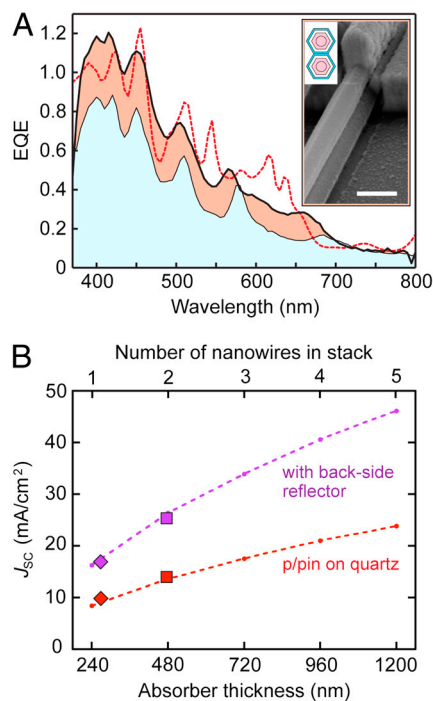

Fig. 5. Vertical assembly of layered NW components for efficient solar cells. (A) Experimental EQE spectrum for double-NW vertical stack (thick black line) and for single-NW (thin black line) device. Both devices are on quartz without back-reflectors. Simulated EQE spectrum for the double-NW stack (dashed red line) using NWs with a Si height of 250 nm. Inset: SEM of a device consisting of two NWs stacked on quartz substrate and electrically connected in parallel; scale bar, 500 nm. (B) Experimental current densities for a single-NW device (diamonds) and stacked double-NW device (squares) under AM 1.5 G 1-sun illumination. Red markers show data without a Ag-metal BSR and purple markers data with the Ag-metal BSR. Dashed red and purple curves denote simulated current densities for stacked NWs with increasing number of NWs in the stack ($N = 1, 2, 3, 4, 5$) without and with a BSR, respectively.

strate. Transport measurements for the vertical stack of two parallel connected p/pin NWs yield a J_{SC} of 14.0 mA/cm^2 (Fig. 5*B*), which represents a 1.4× increase compared to the best single p/pin NW device. Significantly, the experimental EQE spectrum for the stacked double-NW device (Fig. 5*A*) shows that nearly all peaks from 380–700 nm coincide in frequency with those for a single-NW device, and that the EQE amplitudes are increased by a factor of 1.0–2.0 across this wavelength range. These increased amplitudes account for the observed 40% J_{SC} enhancement, and notably, FDTD simulations reproduce the EQE enhancement for the double stack configuration and predict a comparable 41% increase in J_{SC}. Simulations also show that the resonant modes present in a single or in this case the top NW are preserved in the bottom NW, and this effect permits the broadband enhancement observed in the experimental and simulated EQE spectra for the double-NW stack (Fig. S7). In addition, we explored the scaling of our unique concept by simulating NW stack structures with up to five equal diameter NWs and a total thickness of 1.2 μm (Fig. 5*B* and Fig. S7). Comparison of the J_{SC} and EQE for the 5-NW stack and a single microwire with a diameter of the same height shows that the 5-NW stack is predicted to have 26% higher J_{SC} and twofold higher EQE at 620 nm, with the EQE of the stack exceeding that of the microwire for most wavelengths (Fig. S7*B*). Notably, simulations show that a stack of five NWs could yield J_{SC} values of 24 and >40 mA/cm^2 without and with a BSR, respectively, values that could yield power-conversion efficiencies >15%.

Conclusions

Designed 200–300 nm polymorphic core/multishell NWs exhibit excellent photovoltaic properties including high open-circuit voltages up to 0.5 V, ultralow leakage currents of <1 fA, and optimized short-circuit current densities of over 10 mA/cm^2. Large and wavelength tunable nanowire resonant cavity modes lead to light absorption substantially greater than in equivalent thickness thin films, and yield EQE values above unity for specific modes. Optimized devices yield $J_{SC} = 17$ mA/cm^2 and an efficiency of 6%. Integration of multiple devices in parallel demonstrates linear scaling of photocurrent and excellent preservation of device properties, including the high V_{OC}, J_{SC}, and FF values observed in single-NW devices. In addition, we have introduced a unique paradigm for "building" ultrathin photovoltaics through the stacking of designed NW elements, and show that approximately 1 μm thick vertical stacks consisting of 5 NWs could yield efficiencies in excess of 15%. While future studies will be needed to develop further these concepts, we believe that our results demonstrate substantial promise for single and multilayer interconnected assemblies of these core/multishell NW building blocks, including structures tailored to enhance absorption in different regions of the solar spectrum, for the development of next-generation, ultrathin solar cells.

Materials and Methods

Detailed materials and methods can be found in the *Supporting Information*. Briefly, silicon core/multishell NWs were synthesized using our gold-nanocluster catalyzed growth process using SiH_4 as the silicon reactant, B_2H_6 as the p-type dopant and PH_3 as the n-type dopant (8–10); the core and shell structures were grown at 470 and 775 °C, respectively. The structure and phosphorous dopant distribution of NW samples, which were prepared as 40–60 nm thick sections using an ultramicrotome, were characterized by aberration-corrected transmission electron microscopy. NWs were transferred from growth substrates to Si_3N_4 or quartz chips (35), and devices were fabricated by electron beam lithography using Ti/Pd metal contacts. A standard solar simulator with AM 1.5 G filter and calibrated 1-sun intensity was used in conjunction with a probe station and semiconductor parameter analyzer (4156C, Agilent Technologies) to obtain all device transport characteristics. Wavelength-dependent photocurrent spectra were obtained with a home-built optical setup utilizing the solar simulator and a monochromator. Finite-difference time-domain simulations were made for a normally incident plane wave with transverse electric and transverse magnetic orthogonal states, where the absorption cross-section of a NW was obtained by integrating the product of the polarization current density and electric field at each grid point. The absorption cross-section was integrated over one optical period, and the wavelength of the normally incident plane wave was scanned from 280–1000 nm with a step size of 5 nm. The absorption efficiency was defined by the ratio of the NW absorption cross-section to the physical cross-section, and the external quantum efficiency was calculated by multiplying the absorption efficiency by internal quantum efficiency (assumed to be unity).

1. Blankenship RE, et al. (2011) Comparing photosynthetic and photovoltaic efficiencies and recognizing the potential for improvement. *Science* 332:805–809.
2. Hochbaum AI, Yang PD (2010) Semiconductor nanowires for energy conversion. *Chem Rev* 110:527–546.
3. Zhu J, Yu Z, Fan S, Cui Y (2010) Nanostructured photon management for high performance solar cells. *Mater Sci Eng R* 70:330–340.
4. Zhu J, Hsu CM, Yu Z, Fan S, Cui Y (2009) Nanodome solar cells with efficient light management and self-cleaning. *Nano Lett* 9:1979–1984.
5. Wang XD, Song JH, Liu J, Wang ZL (2007) Direct-current nanogenerator driven by ultrasonic waves. *Science* 316:102–105.
6. Tang J, Huo Z, Brittman S, Gao H, Yang PD (2011) Solution-processed core-shell nanowires for efficient photovoltaic cells. *Nature Nanotechnol* 6:568–572.
7. Peng KQ, Lee ST (2011) Silicon nanowires for photovoltaic solar energy conversion. *Adv Mater* 23:198–215.
8. Tian BZ, et al. (2007) Coaxial silicon nanowires as solar cells and nanoelectronic power sources. *Nature* 449:885–889.
9. Kempa TJ, et al. (2008) Single and tandem axial p-i-n nanowire photovoltaic devices. *Nano Lett* 8:3456–3460.
10. Tian B, Kempa TJ, Lieber CM (2009) Single nanowire photovoltaics. *Chem Soc Rev* 38:16–24.
11. Dong Y, Tian B, Kempa TJ, Lieber CM (2009) Coaxial group III-nitride nanowire photovoltaics. *Nano Lett* 9:2183–2187.
12. Kayes BM, Atwater HA, Lewis NS (2005) Comparison of the device physics principles of planar and radial p-n junction nanorod solar cells. *J Appl Phys* 97:114302–114311.
13. Gur I, Fromer NA, Chen CP, Kanaras AG, Alivisatos AP (2007) Hybrid solar cells with prescribed nanoscale morphologies based on hyperbranched semiconductor nanocrystals. *Nano Lett* 7:409–414.
14. Fan ZY, et al. (2009) Three dimensional nanopillar array photovoltaics on low cost and flexible substrates. *Nature Mater* 8:648–653.
15. Chang JA, et al. (2010) High-performance nanostructured inorganic-organic heterojunction solar cells. *Nano Lett* 10:2609–2612.
16. Luther JM, et al. (2007) Multiple exciton generation in films of electronically coupled PbSe quantum dots. *Nano Lett* 7:1779–1784.
17. Cao L, et al. (2009) Engineering light absorption in semiconductor nanowire devices. *Nature Mater* 8:643–647.
18. Cao LY, et al. (2010) Semiconductor nanowire optical antenna solar absorbers. *Nano Lett* 10:439–445.
19. Kamat PV (2008) Quantum dot solar cells Semiconductor nanocrystals as light harvesters. *J Phys Chem C* 112:18737–18753.
20. Colombo C, Heibeta M, Gratzel M, Fontcuberta I, Morral A (2009) Gallium arsenide p-i-n radial structures for photovoltaic applications. *Appl Phys Lett* 94:173108–1–173108–3.
21. Heurlin M, et al. (2011) Axial InP nanowire tandem junction grown on a silicon substrate. *Nano Lett* 11:2028–2031.
22. Kelzenberg MD, et al. (2011) High-performance Si microwire photovoltaics. *Energy Environ Sci* 4:866–871.
23. Putnam MC, et al. (2010) Si microwire-array solar cells. *Energy Environ Sci* 3:1037–1041.
24. Kendrick CE, et al. (2010) Radial junction silicon wire array solar cells fabricated by gold-catalyzed vapor-liquid-solid growth. *Appl Phys Lett* 97:143108–1–143108–3.
25. Yoon HP, et al. (2010) Enhanced conversion efficiencies for pillar array solar cells fabricated from crystalline silicon with short minority carrier diffusion lengths. *Appl Phys Lett* 96:213503-1–213503–3.
26. Garnett E, Yang PD (2010) Light trapping in silicon nanowire solar cells. *Nano Lett* 10:1082–1087.
27. Law M, Greene LE, Johnson JC, Saykally R, Yang P (2005) Nanowire dye-sensitized solar cells. *Nature Mater* 4:455–459.
28. Boettcher SW, et al. (2010) Energy-conversion properties of vapor-liquid-solid-grown silicon wire-array photocathodes. *Science* 327:185–187.
29. Kelzenberg MD, et al. (2010) Enhanced absorption and carrier collection in Si wire arrays for photovoltaic applications. *Nature Mater* 9:239–244.
30. Wadia C, Alivisatos AP, Kammen DM (2009) Materials availability expands the opportunity for large-scale photovoltaics deployment. *Environ Sci Technol* 43:2072–2077.

CHEMISTRY

31. Jeffery LG (2004) *Handbook of Photovoltaic Science and Engineering*, eds S Hegedus and A Luque (Wiley, New York), pp 61–112.
32. Ke Y, et al. (2009) Fabrication and electrical properties of Si nanowires synthesized by Al catalyzed vapor-liquid-solid growth. *Nano Lett* 9:4494–4499.
33. Schmidt V, Wittemann JV, Gosele U (2010) Growth, thermodynamics, and electrical properties of silicon nanowires. *Chem Rev* 110:361–388.
34. Fan ZY, et al. (2008) Wafer-scale assembly of highly ordered semiconductor nanowire arrays by contact printing. *Nano Lett* 8:20–25.
35. Javey A, Nam SW, Friedman RS, Yan H, Lieber CM (2007) Layer-by-layer assembly of nanowires for three-dimensional, multifunctional electronics. *Nano Lett* 7:773–777.